

A Non-rigid Registration Method for Correcting Brain Deformation Induced by Tumor Resection

Yixun Liu¹, *Chengjun Yao², Fotis Drakopoulos¹, Jinsong Wu², Liangfu Zhou² and Nikos Chrisochoides¹

5 ¹The Department of Computer Science, Old Dominion University, Norfolk, VA, USA

²The Department of Neurosurgery, Huashan Hospital, Shanghai, China

*This author contributed equally to the first author.

10 **Correspondence Author**

Professor Nikos Chrisochoides

CRTC Lab and Computer Science, Old Dominion University

E&CS Bldg, 4700 Elkhorn Ave, Suite 3300, Norfolk, VA, 23529

Office phone: (757) 683-7715,

15 Email: nikos@cs.odu.edu

Potential Conflict of Interest

The authors declare that they have no competing interests.

20 **Funding Sources**

This work is funded mainly by the ARRA funds for the ITK-v4 implementation with grant number: NLM A2D2 201000586P. In addition, this work is supported in part by NSF grants: CCF-1139864, CCF-1136538, and CSI-1136536 and by the John Simon Guggenheim Foundation and the Richard T. Cheng Endowment.

25

30

35 **Purpose:** This paper presents a non-rigid registration method to align preoperative MRI (preMRI) with intra-operative MRI (iMRI) to compensate for brain deformation during tumor resection. This method extends traditional point-based non-rigid registration in two aspects: 1) allow the input data to be incomplete, and 2) simulate the underlying deformation with a heterogeneous biomechanical model.

40 **Methods:** The method formulates the registration as a three-variable (point correspondence, deformation field, and resection region) functional minimization problem, in which point correspondence is represented by a fuzzy assign matrix; Deformation field is represented by a piece-wise linear function regularized by the strain energy of a heterogeneous biomechanical model; and resection region is represented by a maximal simply connected tetrahedral mesh. A Nested
45 Expectation and Maximization framework is developed to simultaneously resolve these three variables.

Results: To evaluate this method, we conducted experiments on both synthetic data and clinical MRI data. The synthetic experiment confirmed our hypothesis that the removal of additional elements from the biomechanical model can improve the accuracy of the registration. The clinical MRI experiments
50 on 25 patients showed the proposed method outperforms the ITK implementation of a physics-based non-rigid registration (PBNRR) method. The proposed method improves the accuracy by 2.88 mm on average when the error is measured by a robust Hausdorff distance metric on Canny edge points, and improves the accuracy by 1.56 mm on average when the error is measured by 6 anatomical points.

Conclusions: The proposed method can effectively correct brain deformation induced by tumor
55 resection.

1. INTRODUCTION

Brain deformation severely compromises the fidelity of Image-Guided Neurosurgery (IGNS). Most studies use a biomechanical model to estimate the brain deformation based on sparse intra-operative
60 data after the dura is opened [1-3]. Very few studies address brain deformation during and after tumor resection. The difficulty originates from the fact that resection creates a cavity, which renders the biomechanical model defined on preoperative MRI inaccurate due to the existence of the additional part of the model corresponding to the resection region. In this work, the model accuracy will be improved by 1) removing the tetrahedra in the model corresponding to the resection region and 2)
65 simulating the brain deformation with a heterogeneous biomechanical model. Miga et al. [5] investigated tissue retraction and resection using sparse operating room data and a finite element model. They developed a two-step method: 1) remove tissue volume by manual deletion of model elements that coincide with the targeted zone, and 2) apply boundary conditions to the new surfaces created during the excision process. Determining the cavity is challenging because a portion of it will
70 be filled by surrounding tissues [6]. In this work, we introduced a variable: resection region and

developed a Nested Expectation and Maximization (NEM) framework to automatically resolve it. For convenience, in this paper, we refer to the proposed method as NEMNRR. Based on the Bivariate Demons algorithm, Risholm et al. [8] presented an elastic FEM-based registration algorithm and evaluated it on the registration of 2D pre- with intra-operative images, where a superficial tumor has been resected. Vigneron et al. [21] used the extended finite element method (XFEM) to model surgical cuts, retractions, and resections. XFEM eliminates the computationally expensive re-meshing for the standard finite element method (FEM). The experiment on the simulation of 2D retraction demonstrated the effectiveness of this method. Ding et al. [6] presented a semi-automatic method based on post-brain tumor resection and laser range data. Vessels were identified in both preoperative MRI and laser range image, and then the Robust Point Matching (RPM) method [9] was used to force the corresponding vessels to exactly match each other under the constraint of the bending energy of the whole image. RPM uses Thin-Plate Splines (TPS) as the mapping function. The basis function of TPS is a solution of the biharmonic [10], which does not have a compact support and will therefore lead to, in real applications, unrealistic deformation in the region far away from the matching points. In other words, TPS is not suitable for estimating deformation with sparse data. We used a heterogeneous biomechanical model to realistically simulate the underlying movement of the brain, which extended our previous work using a homogeneous model [19]. Clatz et al. [16] presented a physics-based non-rigid registration (PBNRR) method to deal with the registration between the preMRI and iMRI. We completely implemented this method in ITK [35, 36]. PBNRR used a homogeneous biomechanical model to estimate the entire brain deformation. In this work, we introduced a heterogeneous model into the registration and enabled the removal of the portion of the model corresponding to the resected tumor. Risholm et al. [37] presented a registration framework accommodating resection and retraction based on the bivariate Demons algorithm. Retraction is detected at areas of the deformation field with high internal strain, and resection is detected by a level set method evolving in the space where image intensities disagree. Their preliminary results on both synthetic and clinical data showed the added value of explicitly modeling these processes in a registration framework. Periaswamy et al. [38] presented an intensity-based registration method dealing with partial data, in which the transformation was modeled as locally affine but globally smooth, and the Expectation and Maximization (EM) algorithm served to estimate the missing or partial data. Their work was not directly related with tumor resection but motivated us to use EM strategy to deal with tumor resection.

In this paper, we present a point-based NRR method, which is characterized by using a heterogeneous biomechanical model to simulate the underlying deformation and using a Nested EM strategy to remove point outliers and element outliers.

2. METHODS AND MATERIALS

In this section, we present the details of the proposed registration method and the experimental data for the evaluation. We begin from a complete flowchart to describe the entire procedures of aligning preoperative MRI and intra-operative MRI. Then, we briefly describe a multi-tissue mesh generation method, which serves to build a heterogeneous biomechanical model in the registration method. Next, we present the details of the proposed registration method including the derivation of the cost function and the Nested Expectation and Maximization solver. Finally, the synthetic data and the clinical MRI data are presented.

Figure 1 illustrates the complete flowchart to align preoperative MRI with intra-operative MRI. In this paper, we focus on the Nested Expectation and Maximization non-rigid registration (NEMNRR) component highlighted with a blue color. For self-containedness, we also briefly describe our multi-tissue mesh generation presented in [4, 40].

The brain was automatically extracted from the skull by a Brain Extraction Tool (BET) [22], and the ventricle was segmented by a region growing method in 3DSlicer [23]. The resulting two-tissue (brain and ventricle) multi-label image was fed into a multi-tissue mesher to produce a heterogeneous model in conjunction with specific biomechanical attributes. Edge detection was performed on both pre- and intra-operative MRI to produce a source point set and a target point set. Classic Canny edge detection, facilitated by an open source tool ITK [24], was employed to produce these two point sets.

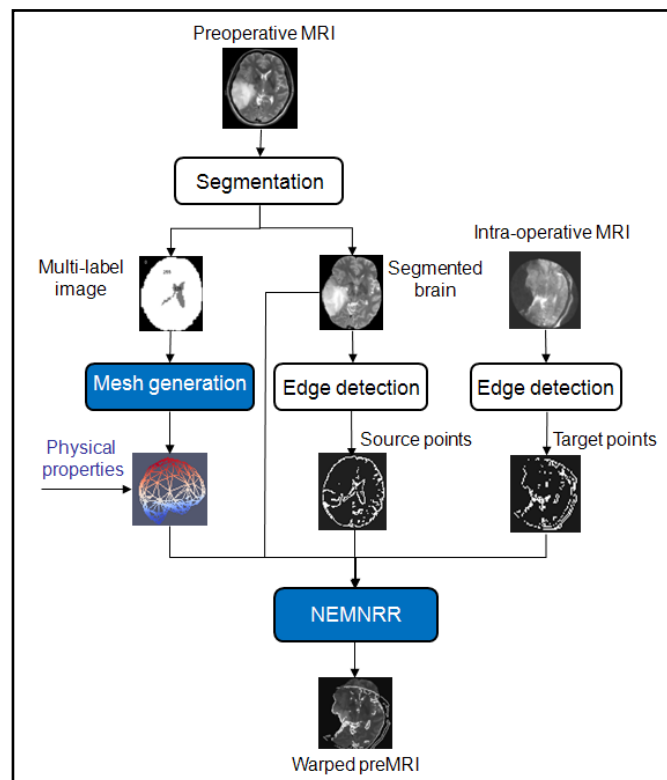


Figure 1. The complete flowchart to align preoperative MRI with intra-operative MRI, in which only the highlighted Mesh generation and NEMNRR are addressed in this paper.

130 The feature point-based non-rigid registration problem addressed in this paper can be stated as:
Given a source point set in preoperative MRI and a target point set in intra-operative MRI, find the point correspondence, deformation field, and resection region.

We resolve this problem by incorporating all three variables into a single cost function, which is minimized by a Nested EM strategy. A displacement vector defined on the mesh nodes represents the deformation field; a correspondence matrix represents the correspondence between two point sets; and
135 a connected submesh represents the resection region. Our Nested EM method does not require the correspondence to be known in advance and allows the input images to be incomplete, thereby making this method a generalized point-based registration method. Moreover, to improve the accuracy, a heterogeneous biomechanical model serves to realistically simulate the underlying
140 movement of the brain. This heterogeneous model includes a multi-tissue mesh and specific biomechanical attributes of each tissue.

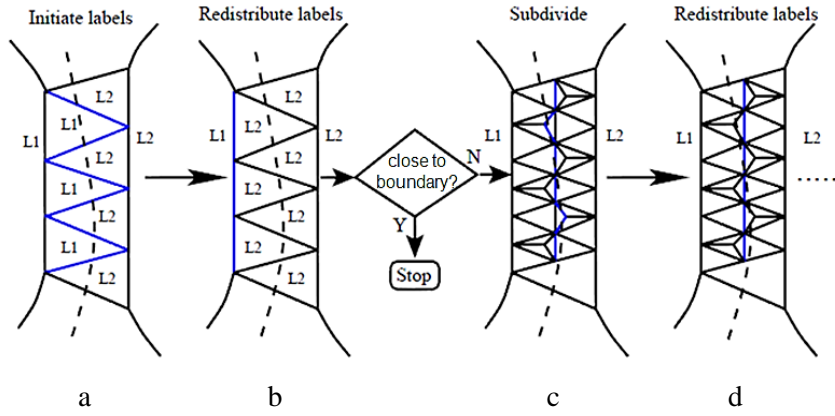
In the following subsections, we first briefly describe the multi-tissue mesh generation method; then derive the cost function step by step; finally present a Nested EM strategy to resolve this cost function.

145 **2.1 Multi-tissue Tetrahedral Mesh Generation**

A biomechanical brain model is able to realistically describe the deformation of the entire brain based on sparse information. A heterogeneous model is more realistic than a homogeneous model, but necessitates a multi-tissue mesher. Given a multi-label brain image as input, the multi-tissue mesher should discretize the entire brain to connected tetrahedra. In a multi-tissue mesh, each tetrahedron is
150 assigned with a tissue label based on the tissue in which the volume fraction of the element is the largest. The interface of any two submeshes is well aligned with the tissue boundary defined in the multi-label image. In this section, we describe our previous work on a multi-tissue mesher [4, 40]. The multi-tissue mesher consists of two steps: 1) start from a homogeneous Body-Centered Cubic (BCC) mesh [25, 26] to identify a coarse multi-tissue mesh by assigning each tetrahedron with a
155 specific tissue label, and 2) deform the coarse multi-tissue mesh surfaces to tissue boundaries defined in the multi-label image.

2.1.1 Generate a coarse multi-tissue mesh

BCC mesh is an actual crystal structure ubiquitous in nature. The nodes of BCC are grid points of two interlaced grids. The edges of BCC consist of edges of the grid and additional edges between a node
160 and its eight nearest neighbors in the other grids. The advantage of the BCC mesh is that it is highly structured and easily refined during the simulation after subdivision [26]. Label distribution is performed on the homogeneous BCC mesh to produce a coarse multi-tissue mesh, which is deformed subsequently to the real tissue boundaries identified in the multi-label image.



165

170

Figure 2. Coarse multi-tissue mesh generation. (a) L1 and L2 are tissue labels; the dashed line is the real boundary; and the blue line is the submesh interface. (b) Redistribution of labels. (c) Subdivision of tetrahedra if the submesh interface is not close enough to the real boundary. (d) Redistribution of labels again.

175

Given an initial label assignment (Figure 2a), labels are redistributed to produce a surface robust (not zigzag) against deformation (see the blue line in Figure 2b). If the surface is not close enough to the tissue boundary (dashed line in Figure 2b), mesh subdivision will be performed on the tetrahedra across the tissue boundary as shown in Figure 2c. The subdivision might impair the robustness of the surface. In this case, label redistribution is performed to produce a surface that is robust and better approximates the tissue boundary (see Figure 2d). The above procedures are repeated until the multi-tissue surface is well-posed for deformation and close enough to the tissue boundary.

2.1.2 Deform the coarse multi-tissue mesh surface to the tissue boundary

180

To make the mesh surface conform to the tissue boundary, the coarse multi-tissue mesh surface is iteratively deformed to the tissue boundary by moving surface nodes with a displacement vector U , which is resolved by minimizing,

$$W(U) = \sum_{i=1}^n (U^T K_i U + \lambda \|H_i U - D_i\|^2) \quad (1)$$

185

n is the number of tissues; K_i is the global stiffness matrix assembled by the elements within the i -th tissue. K_i depends on two biomechanical attributes of the i -th tissue: Young's modulus and Poisson's ratio. The building of K_i has been well-documented in [12]. H_i is the global linear interpolation matrix related to the registration points or source points within the i -th tissue. In the next subsection, we will present the assembly of H_i . D_i is the global displacement vector from the i -th mesh surface to the i -th tissue boundary. λ controls the balance of the quality (the first term) and the fidelity (the second term). U can be resolved by a linear system of equations,

$$\frac{\partial W}{\partial U} = 0 \Rightarrow \sum_{i=1}^n (K_i + \lambda H_i^T H_i) U = \sum_{i=1}^n \lambda H_i^T D_i \quad (2)$$

190

195 In energy function (1), the second terms is used to match the mesh surface to the tissue boundary. To control the mesh quality while deforming the mesh surface, we introduce a biomechanical model and use the strain energy of the model (Finite Element representation) as the regularization (the first term). The strain energy is a measure of the magnitude of the mesh deformation. As a result, the resulting mesh obtained by minimizing function (1) is a trade-off of the boundary matching and the mesh quality. To improve the performance of the multi-tissue mesher, we model the brain as a heterogeneous biomechanical model, in which each tissue is characterized by biomechanical attributes. The mesh surface is determined by the label of the tetrahedral elements. For each element, if its volume fraction inside tissue i is the largest, this element is assigned label i . The interface of two
 200 tissues is determined by looping all element surfaces to check if the surface is shared by two elements with different labels.

Mesh quality control is one advantage of our multi-tissue mesher [4, 40]. Mesh quality is the measure of how well the elements of a mesh are shaped. Mesh quality can be evaluated using different metrics, such as the minimal dihedral angle, aspect ratio, etc. Mesh quality influences the accuracy and convergence of the finite element solver as demonstrated in our previous work [34]. For example, if the angle between two triangles of a tetrahedron is very small, the assembled stiffness matrix will be ill-conditioned, characterized by a larger condition number (a measure of the asymptotically worst case of how much the error can be magnified in proportion to a small error). This characteristic of “magnifying the error” of an ill-conditioned matrix severely deteriorates the convergence of a linear
 205 system of equations, especially when the linear system is solved iteratively.
 210

2.2 Nested Expectation and Maximization Non-rigid Registration (NEMNRR)

We treat the registration as an optimization problem, which includes three variables: point correspondence, deformation field, and resection region. In this section, we first derive a cost function to incorporate these three variables. To make the derivation easily to be followed, we start from a simple point-based non-rigid registration cost function with an analytical format, and then gradually derive our cost function by relaxing the requirement for the point correspondence, incorporating a heterogeneous model and discretizing with Finite Element Method. To resolve the cost function, we present a Nested Expectation and Maximization algorithm to iteratively estimate the three variables.
 215

2.2.1 Cost function

220 Given a source point set $S = \{s_i\}_{i=1}^N \in R^3$ and a target point set $T = \{t_i\}_{i=1}^N \in R^3$ with known correspondence (i.e., s_i corresponds to t_i), the point-based non-rigid registration problem can be formulated as the minimization of the functional,

$$J(u) = \int_{\Omega} R(u) d\Omega + \lambda \sum_{s_i \in \Omega} \|s_i + u(s_i) - t_i\|^2 \quad (3)$$

where u is the unknown deformation field. The first term is smoothing energy for regularization, and the second term is similarity energy. λ controls the trade-off between these two terms. Ω is the problem domain, namely the segmented brain of preoperative MRI, in the brain MRI registration. The tumor resection influences Ω , and therefore influences both terms of functional (3). We introduce a variable Ω' to represent the resection region in preoperative MRI corresponding to the resection region in iMRI. To relax the requirement of one-to-one correspondence between S and T , we introduce variable c_{ij} to represent the degree to which point s_i corresponds to t_j . To reach realistic deformation, the general regularization term of functional (3) is specified as the strain energy of a linear elastic homogeneous model. As a result, functional (3) changes to,

$$J(u, c_{ij}, \Omega') = \int_{\Omega \setminus \Omega'} \sigma(u) \varepsilon(u) d(\Omega \setminus \Omega') + \lambda_1 \sum_{s_i \in \Omega \setminus \Omega'} \left\| s_i + u(s_i) - \sum_{t_j \in \Omega_R} c_{ij} t_j \right\|^2 + \lambda_2 \iiint_{\Omega'} d(\Omega') \quad (4)$$

$\sigma(u)$ is the stress tensor, and $\varepsilon(u)$ is the strain tensor. Their tensor product represents strain energy. d is the differential sign. The c_{ij} is defined as in RPM [27] with soft assignment, which is suitable for non-rigid registration. The classic Iterative Closest Point (ICP) method [28] treats the correspondence as a binary variable and assigns the value based on the nearest-neighbor relationship; however, this simple and crude assignment is not valid for non-rigid registration, especially when large deformation and outliers are involved [27]. We define a search range Ω_R , a sphere centered at the source point with a radius R , and only take into account: 1) the target points, which are located in Ω_R of the source point, and 2) the source points, which have at least one target point in Ω_R . Thus, with this simple extension of RPM, the method is capable of eliminating outliers existing in both point sets. In functional (4), the first two terms come from the extension of functional (3), and the last term serves to prevent a too large resection region from being rejected. Without the last term, the entire Ω might be rejected as the outlier, leading to the vanishing of the integral domain.

The homogeneous model employed in the regularization term of functional (4) is further extended to a heterogeneous model,

$$J(u, c_{ij}, \Omega') = \sum_{\Omega_i \in \Omega \setminus \Omega'} \int_{\Omega_i} \sigma_i(u) \varepsilon_i(u) d\Omega_i + \lambda_1 \sum_{s_i \in \Omega \setminus \Omega'} \left\| s_i + u(s_i) - \sum_{t_j \in \Omega_R} c_{ij} t_j \right\|^2 + \lambda_2 \iiint_{\Omega'} d(\Omega') \quad (5)$$

where $\cup \Omega_i = \Omega \setminus \Omega'$, $i = 1 \dots n$. Ω_i is the i -th tissue domain and n is the number of tissues. $\sigma_i(u) \varepsilon_i(u)$ represents the strain energy associated with the i -th tissue.

Remark: If $n = 1, \Omega' = \emptyset, c_{ij} = \begin{cases} 1 & i = j \\ 0 & \text{otherwise} \end{cases}$, then functional (5) is reduced to functional (3),

250 which means the proposed method might be viewed as a generalized point-based NRR method characterized by 1) employing a heterogeneous biomechanical model as the regularization term, 2) accommodating incomplete data, and 3) without correspondence requirement.

Functional (5) is approximated by function (6) using the finite element method,

$$J(U, C, M_{Rem}) = \sum_{e_i \in M \setminus M_{Rem}} U^T K_{e_i} U + \lambda_1 \sum_{s_i \in M \setminus M_{Rem}} (HU - D(C))^T W (HU - D(C)) + \lambda_2 \sum_{e_i \in M_{Rem}} V_{e_i} \quad (6)$$

The continuous domain Ω is discretized as a multi-tissue mesh M using the multi-tissue mesh generation method presented in Section 2.1 on a multi-label image segmented from the preoperative MRI. M_{Rem} is the removed mesh approximating the resection region Ω' . K_{e_i} is the element stiffness matrix of element e_i . Each element is associated with a tissue label, which determines the elastic parameters to build the element stiffness matrix. The first term of equation (6) approximates the strain energy as in [12, 20], and the third term approximates the volume of the resection region, in which V_{e_i} is the volume of element e_i . In the second term, the entries of the vector D are defined as $d_i(c_{ij}) = s_i - \sum_{t_j \in \Omega_R} c_{ij} t_j, \forall s_i \in M \setminus M_{Rem}$. The equation to calculate c_{ij} will be given in Section 2.2.2.a. C is a point correspondence matrix with entries c_{ij} . W in the second term is a weighted matrix of size $3|S| \times 3|S|$. W is a block-diagonal matrix whose 3×3 submatrix W_k is defined as $\frac{m}{|S|} S_k^{avg}$, where m is the number of the vertices of the mesh. $\frac{m}{|S|}$ makes the matching term independent of the number of the vertices and the registration (source) points. S_k^{avg} is the average stiffness tensor for the k -th registration point. S_k^{avg} makes the registration point act as an elastic node of the finite element model, leading to the same measurement unit of the regularization and matching terms of function (6) (without W , the matching term has a unit mm^2 , which is different from $Force \times Distance$ in the regularization term).

270 Assume the k -th registration point is located in the tetrahedron defined by vertices $c_i, i \in [0:3]$. S_k^{avg} is calculated by $S_k^{avg} = \sum_{i=0}^3 h_i K_{c_i}$, where K_{c_i} is a 3×3 sub-matrix of the global stiffness matrix K . h_i is the interpolation factor, the element of the global linear interpolation matrix H [16]. H is assembled by accumulating contributions of all registration points as follows:

275 The k -th registration point o_k contained in the tetrahedron defined by vertices $c_i, i \in [0:3]$ contributes to four 3×3 sub-matrices: $[H]_{k_{c_0}}, [H]_{k_{c_1}}, [H]_{k_{c_2}}, [H]_{k_{c_3}}$. The diagonal matrix $[H]_{k_{c_i}} = \text{diag}(h_i; h_i; h_i)$, in which the linear interpolation factor h_i is calculated as,

$$\begin{bmatrix} h_0 \\ h_1 \\ h_2 \\ h_3 \end{bmatrix} = \begin{bmatrix} v_{c_0}^x & v_{c_1}^x & v_{c_2}^x & v_{c_3}^x \\ v_{c_0}^y & v_{c_1}^y & v_{c_2}^y & v_{c_3}^y \\ v_{c_0}^z & v_{c_1}^z & v_{c_2}^z & v_{c_3}^z \\ 1 & 1 & 1 & 1 \end{bmatrix}^{-1} \begin{bmatrix} o_k^x \\ o_k^y \\ o_k^z \\ 1 \end{bmatrix} \quad (7)$$

where v_{c_i} is the mesh node with index c_i .

H is also used in mesh deformation, the second step of multi-tissue mesh generation (see Section 2.1.2). In mesh deformation, because we use the mesh nodes as registration points (i.e., o_k is the same as one of the four tetrahedron nodes), equation (7) is reduced to,

$$h_i = \begin{cases} 1 & o_k = v_{c_i} \\ 0 & otherwise \end{cases} \quad (8)$$

Finding correspondence matrix C and removed mesh M_{Rem} is equivalent to outlier rejection. We developed a Nested Expectation and Maximization strategy to iteratively reject point and element outliers.

2.2.2 Nested Expectation and Maximization strategy

The Expectation and Maximization (EM) algorithm [7] is a general algorithm for maximum-likelihood [13] estimation of model parameters (unknowns) in the presence of missing or hidden data. EM proceeds iteratively to estimate the model parameters. Each iteration of the EM algorithm consists of two steps: the E step and the M step. In the E step, the missing data is estimated given the observed data and current estimate of the model parameters. In the M step, the likelihood function is maximized under the assumption that the missing data is known. The estimate of the missing data from the E step is used in lieu of the actual missing data. Convergence is assured since the algorithm is guaranteed to increase the likelihood at each iteration [7].

Considering the registration problem in the EM context, cost function (6), from the probability (Bayesian) point of view, defines the likelihood function, in which the unknown (model parameter) is the displacement vector U , and the missing data are the correspondence C and the resection region M_{Rem} . Assuming M_{Rem} is known, the more accurate the estimate of C , the more accurate the estimate of U , and vice versa. EM algorithm is very efficient for this kind of circular dependence problems [7, 27, 37], so we employ EM to solve U and C under a specified M_{Rem} . To resolve M_{Rem} , we treat U and C as an unknown pair $\langle U, C \rangle$. The more accurate the estimate of M_{Rem} , the more accurate the estimate of $\langle U, C \rangle$, leading to a Nested EM framework as shown in Figure 3, in which the inner EM serves to resolve $\langle U, C \rangle$ with M_{Rem} fixed, and the outer EM serves to resolve M_{Rem} . M_{Rem} is approximated by a collection of tetrahedra located in a region of the model, which corresponds to the resection region in the intra-operative MRI. M_{Rem} is initialized to \emptyset and updated at each iteration of the outer EM. If all the tetrahedra contained in the resection region are collected, the outer EM stops.

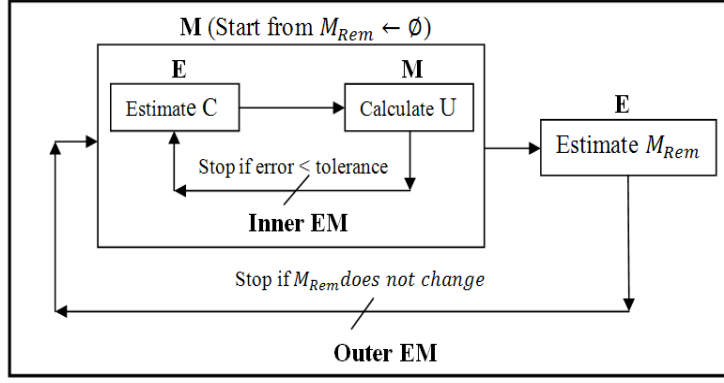


Figure 3. Nested Expectation and Maximization framework.

310

a) *Inner EM*: Inner EM is used to resolve $\langle U, C \rangle$ given M_{Rem} . For each source point s_i , assume its correspondences are subject to Gaussian distribution [27], so c_{ij} can be estimated (E step) by,

$$c_{ij} = \frac{c'_{ij}}{\sum_{k=1}^m c'_{ik}}, c'_{ij} = \frac{1}{R\sqrt{2\pi}} e^{-\frac{(t_j - s_i)^2}{2R^2}}, \forall t_j \in \Omega_R, j = 1 \dots m \quad (9)$$

Once C is estimated, U can be resolved by solving a linear system of equations resulting from setting the derivative of function (6) to zero, i.e., $dJ/dU = 0$. The resolved U is used to warp S closer to T , and then the correspondence matrix C can be updated. The pseudo code of the inner EM is presented in Algorithm 1.

315

b) *Outer EM*: Outer EM is used to identify M_{Rem} . In M step, the inner EM resolves $\langle U, C \rangle$. In E step, an element outlier rejection algorithm resolves M_{Rem} . M_{Rem} is approximated by a collection of tetrahedron outliers, which fall in the resection region of the intra-operative MRI.

320

The resection region does not need to be identified in the intra-operative MRI, and in fact it is hard to distinguish the resection region from the background; however, a simple threshold segmentation method can very easily segment the background image BGI including the resection region and the background. We cannot determine if a tetrahedron is an outlier based only on whether it is located in the BGI because this tetrahedron might happen to fall in the background rather than the resection region. To make the element outlier rejection algorithm robust, we utilize the fact that the resection region is a collection of tetrahedra, which not only fall in the BGI of intra-operative MRI, but also connect with each other and constitute a maximal simply connected submesh. The collection of the outliers proceeds iteratively, and at each iteration, or more specifically in the E step of outer EM, additional outliers will be added into M_{Rem} if they fall in the BGI and connect with the maximal simply connected submesh identified in the previous iteration. The element outlier rejection algorithm is presented in Algorithm 2.

325

330

$$[U, C] = \text{PointOutlierRejection} (M, M_{Rem}, S, T, \varepsilon, r, R)$$

Inputs: M : non-resected mesh, M_{Rem} : resected mesh, S : source points,

T : target points, ε : tolerance, r : annealing rate, R : search range

340

Outputs: U : displacement vector, C : correspondence matrix

1: $U \leftarrow I$ // identify transform

2: **repeat**

3: Transform S based on U : $S \leftarrow U(S)$

345

4: E-Step:

5: // outlier rejection for S

6: $S \leftarrow S \setminus \{s_i \mid \text{if no target points in } \Omega_R\}$

7: // outlier rejection for T

8: $T \leftarrow T \setminus \{t_i \mid \text{if no source points listing it within } \Omega_R\}$

350

9: Estimate correspondence C using equation (9)

10: M-Step:

11: Solve U by minimizing function (6)

12: $error \leftarrow \|U_i - U_{i-1}\|$

13: Decrease R : $R \leftarrow R \times r$

355

14: **until** $error < \varepsilon$

Algorithm 1. Point outlier rejection.

The outer EM iteratively rejects element outliers using Algorithm 2 and computes $\langle U, C \rangle$ using
 360 Algorithm 1 until no additional element outliers are detected. We illustrate this NEM strategy in
 Figure 4, in which the inner EM iterates along the horizontal direction, and the outer EM iterates
 along the vertical direction. In Figure 4, we use subscript i to denote the inner EM and subscript o to
 denote outer EM. The superscript is used to denote the iteration number. For example, E_i^k denotes the
 365 k -th iteration of E step in the inner EM. The blue boundary in Pre-op MRI represents the resection
 surface corresponding with the resection surface of iMRI. In the horizontal direction, inner EM
 iteratively estimates the correspondence and deformation field until no point outliers are detected.
 Inner EM begins from a search range (green circle) with a larger radius R . For each source point, if
 there are no target points located in the circle centered at the source point, this source point will be
 rejected as an outlier. For each target point, if it is outside of the search range, this target point will be
 370 rejected as an outlier. Once all the outliers are rejected, C can be estimated by equation (9), and U can
 be solved by minimizing function (6) (see Algorithm 1). Then, M_{Rem} can be detected using Algorithm

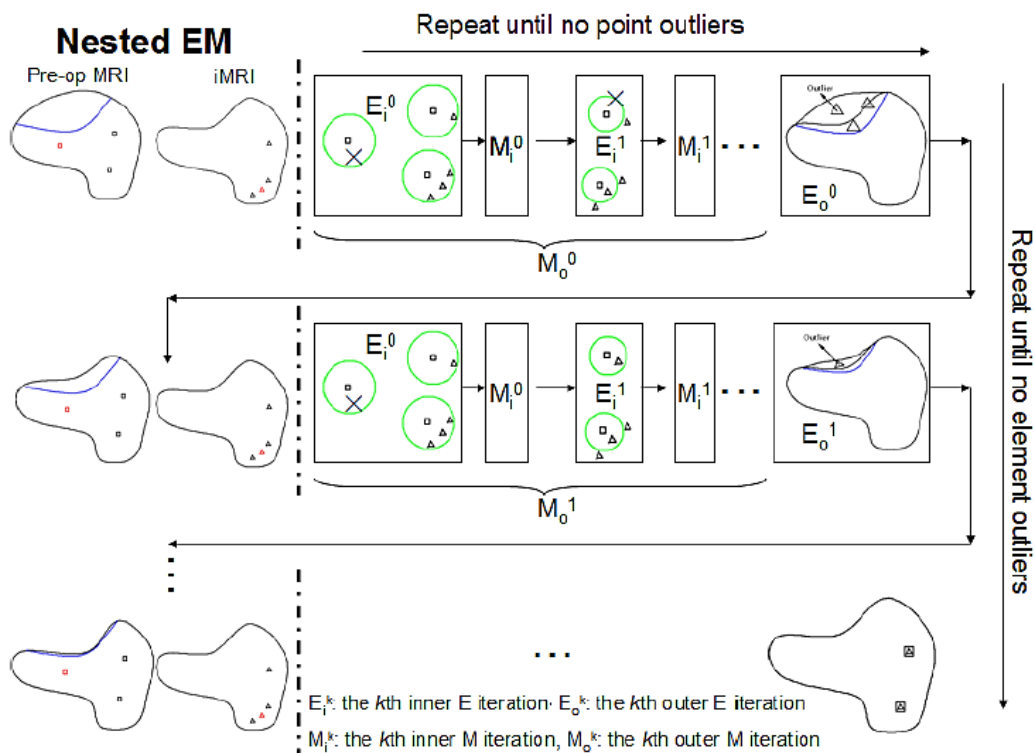
2. The M_{Rem} is removed from the pre-op MRI and the model leading to a resection surface close to the real resection surface (blue boundary) for the next iteration. In the next iteration, search radius R is reduced by multiplying with a simulated annealing factor 0.93 suggested in [27, 13], M_{Rem} is removed from M , and the above procedure is repeated. Algorithm 3 presents the whole pseudo code of the NEMNRR.

$[M_{Rem}, S] = \text{ElementOutlierRejection}(M, M_{Rem}, U, BGI, S)$

380 **Inputs:** M : non-resected mesh, M_{Rem} : removed mesh,
 U : displacement vector, BGI : background image, S : source points
Outputs: M_{Rem} : new removed mesh, S : new source points

- 385 1: Obtain deformed resected mesh $M_{Def} \leftarrow U(M \setminus M_{Rem})$
2: Find all elements M_1 completely contained in the background Image BGI and constitute the largest connected mesh with M_{Rem}
3: Map M_1 in M_{Def} to M_2 in $M \setminus M_{Rem}$
4: $M_{Rem} \leftarrow M_{Rem} \cup M_2$
5: $S \leftarrow S \setminus \{s_i \mid s_i \in M_{Rem}\}$
-

390 Algorithm 2. Element outlier rejection.



395 Figure 4. Illustration of Nested Expectation and Maximization strategy. Horizontal direction: inner EM, Vertical
direction: outer EM. In the horizontal direction, each inner EM gradually detects the element outliers (resection
region) and then removes them from the pre-op MRI. In the vertical direction, the resulting resection surface
gradually approaches the real resection boundary (blue boundary).

400

$[U, M_{Rem}, C] = NEMNRR(preMRI, iMRI)$

Input: *preMRI*: preoperative MRI, *iMRI*: intra-operative MRI

Output: *U*: displacement vector, *M_{Rem}*: resected mesh,

405

C: correspondence matrix

1: Segment brain in *preMRI* and do mesh generation to produce *M*

2: Segment background image *BGI* in *iMRI*

3: Canny edge detection in *preMRI* to get *S*

4: Canny edge detection in *iMRI* to get *T*

410

5: Initialize *R*, ϵ , and *r*

6: Initialize $M_{Rem} \leftarrow \emptyset$

7: **repeat**

8: M-Step:

$[U, C] \leftarrow PointOutlierRejection(M, M_{Rem}, S, T, \epsilon, r, R)$

9: E-Step:

415

$[M_{Rem}, S] \leftarrow ElementOutlierRejection(M, M_{Rem}, U, BGI, S)$

10: **until** M_{Rem} does not change

Algorithm 3. Nested Expectation and Maximization non-rigid registration.

420 **2.3 Experimental Data**

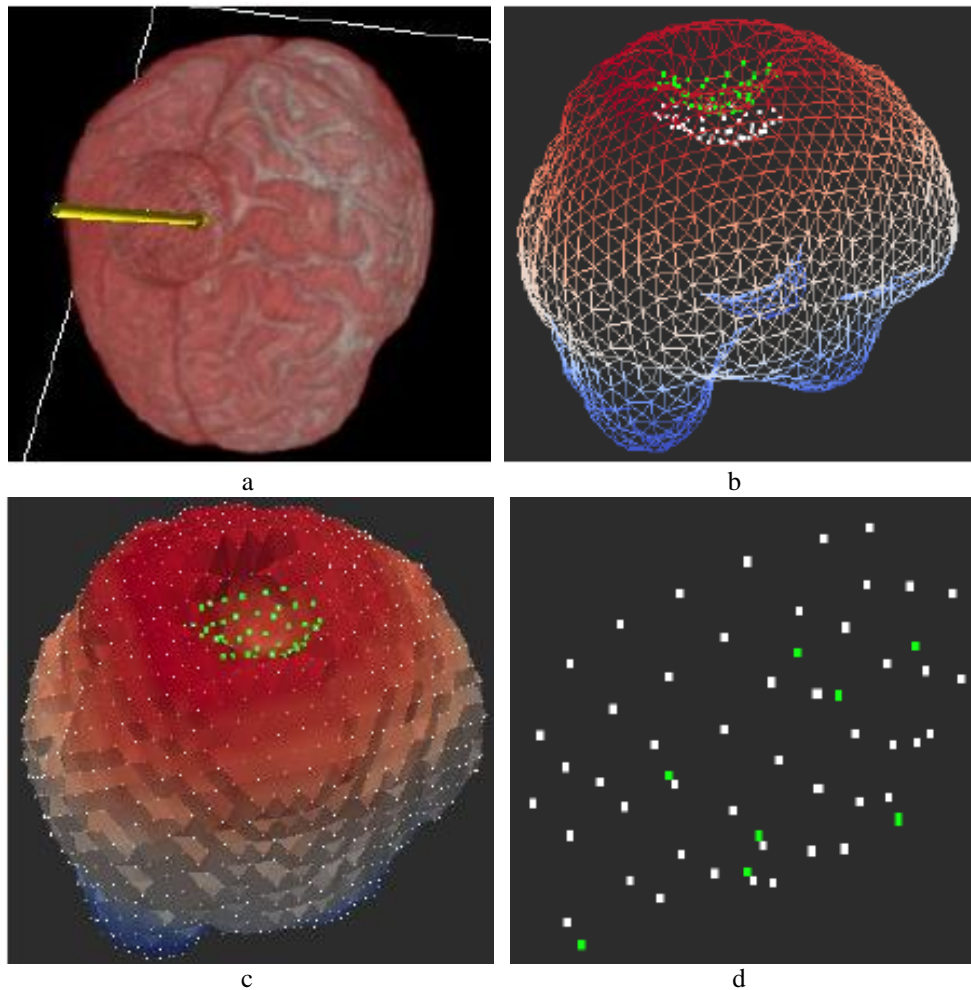
To evaluate the proposed method, we conducted experiments on both synthetic and clinical data. The
synthetic data serves to evaluate our hypothesis that *the removal of the resection region can improve*
the accuracy of the registration, and the clinical data serves to evaluate the accuracy of the proposed
method.

425

2.3.1 Synthetic data

To generate a synthetic resected brain, we developed a surgery simulation tool to simulate brain
resection as shown in Figure 5a. To produce the synthetic data, about 1/27 brain volume is removed,
and the resected surface is deformed with a magnitude of 10 mm along the direction from top to the

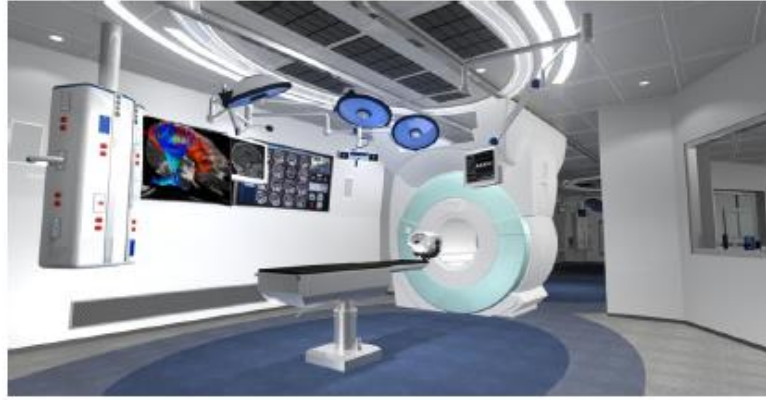
430 bottom of the brain. The synthetic deformed resected brain is produced by our surface-based
registration tool [29, 30], which is capable of deforming the brain based on a specific boundary
condition: the deformation of the resection surface. The source points S are simulated as the surface
nodes of the resection region (green points in Figure 5b) before deformation, and the target points T
(white points in Figure 5b) are the surface nodes of the resection region after deformation. All the
435 surface nodes except the green nodes are added into S as the outliers (white points in Figure 5c). The
outliers for T are generated using white Gaussian noise (green points in Figure 5d).



440
Figure 5. Synthetic data. (a) Surgery simulation. (b) Source (green) and target points (white). (c) Source points
(green) with outliers (white). (d) Target points (white) with noises (green).

445 2.3.2 Clinical data

The proposed method was evaluated using 25 clinical volume MRI data. The Surgical Planning Laboratory (SPL), Harvard Medical School [31, 32] provided the first 10 cases and the Department of Neurosurgery at Shanghai Huashan Hospital (Figure 6) provided the rest 15 cases.



450 Figure 6. The 3.0 T magnet system (Signa SP, Siemens Medical Systems) of the Neurosurgery Department of Huashan Hospital, Shanghai, China

455 Table 1. Patient information of 25 clinical MRI cases. The first 10 cases were provided by SPL, and the rest 15 cases by the Neurosurgery Department, Huashan hospital, China.

| Case | gender | Tumor Location | Histopathology |
|------|--------|----------------------|---|
| 1 | M | L perisylvian | Oligoastrocytoma WHO II/IV |
| 2 | M | fronto-temporal | Oligodendroglioma WHO II/IV |
| 3 | F | R occipital | Anaplastic Oligodendroglioma WHO III/IV |
| 4 | N/A | L frontal | Oligodendroglioma WHO II/IV |
| 5 | F | L frontal | Glioblastoma multiforme (WHO IV/IV) |
| 6 | N/A | R frontal | Oligodendroglioma WHO II/IV |
| 7 | N/A | R occipital | N/A |
| 8 | F | R frontal | Oligoastrocytoma WHO II/IV |
| 9 | F | L Parietal | Glioblastoma multiforme (WHO IV) |
| 10 | M | L frontal | Glioblastoma multiforme (WHO IV) |
| 11 | M | R temporal | Metastases |
| 12 | F | L posterior temporal | Oligodendroglioma WHO II |
| 13 | F | L frontal | Glioma |
| 14 | F | L frontal | Glioma |
| 15 | M | L frontal | Glioma |
| 16 | M | L frontal | Glioma |
| 17 | M | R frontal | Glioma |
| 18 | M | R parietal | Glioma |
| 19 | F | R frontal | Glioma |
| 20 | M | L frontal | Glioma |
| 21 | N/A | N/A | N/A |
| 22 | M | L frontal | Glioma |
| 23 | M | L frontal | Glioma |
| 24 | F | L frontal | Glioma |
| 25 | F | L frontal | Glioma |

Table 1 lists all patient information including the gender, tumor location, and histopathology. The MRI data of the first 10 cases were acquired with the protocol: whole brain sagittal 3D-SPGR (slice

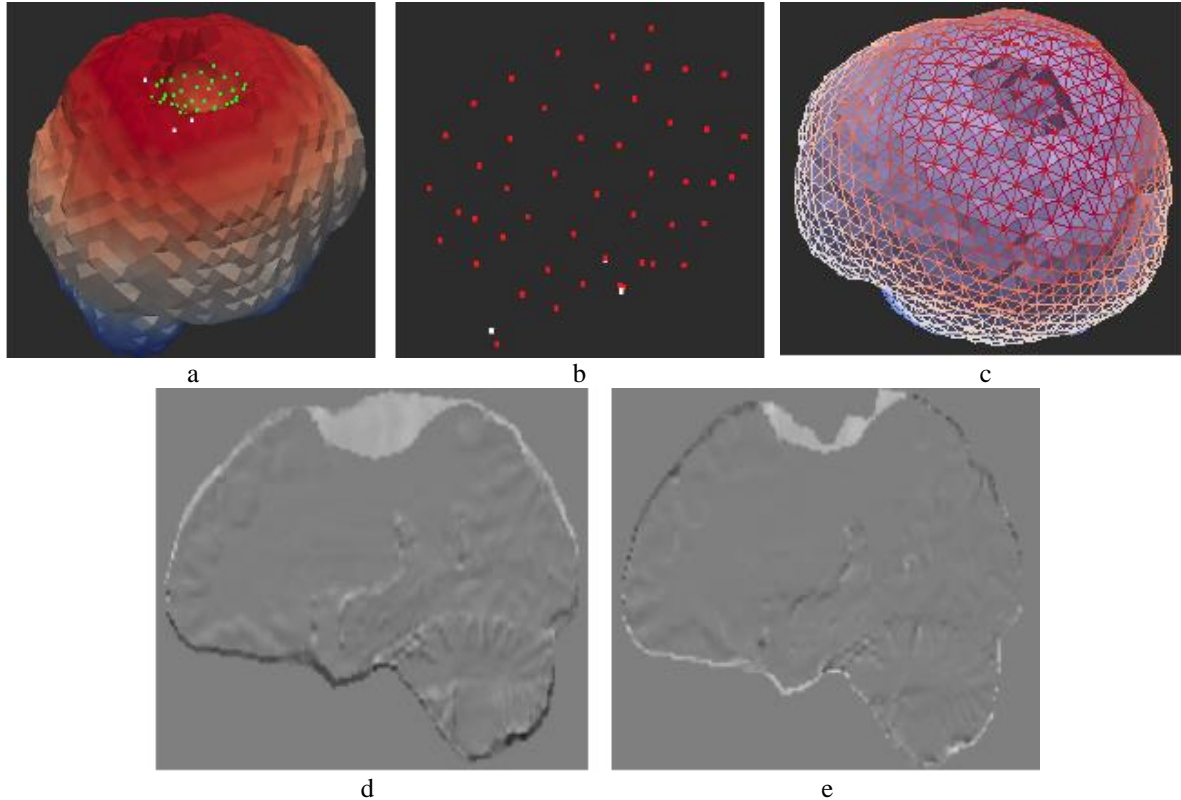
460 thickness 1.3 mm, TE/TR=6/35 ms, FA=75°, FOV=24 cm, matrix=256 × 256). For the rest 15 cases of Huashan hospital, the MRI data were acquired (IMRISneuro, IMRIS, Canada) in 8 minutes with the protocol: 3D T1-weighted magnetization-prepared rapid gradient echo (MPRAGE) sagittal images with [dimension = 256 × 256 × 176, in plane resolution = 1.0 × 1.0 mm, thickness = 1.0 mm, FOV = 256 × 256].

465 3. RESULTS

In this section, we first evaluate the proposed NEMNRR method on both synthetic data and clinical MRI data and then compare the proposed NEMNRR with a classic point-based NRR: PBNRR.

3.1 Experiments on Synthetic Data

470 Figure 7a and Figure 7b show that Algorithm 1 correctly detects all the source points and target points. Most outliers are rejected from S and T except three outliers in S (white points in Figure 7a) and corresponding three outliers in T (white points in Figure 7b). Figure 7c shows the mesh with element outliers removed, i.e., $M \setminus M_{Rem}$, produced by Algorithm 2. We purposely put the non-resected mesh M and the resected mesh $M \setminus M_{Rem}$ together to show the resection region clearly. We conducted an
475 experiment to verify our hypothesis: *the removal of element outliers from the model can improve the accuracy of the registration*. In the experiment, we registered the non-resected brain with the synthetic deformed resected brain with and without rejecting element outliers. In both registrations, we used the same source points and target points. So, the removal of element outliers or not is the unique reason causing variation of the results. For each registration, the registration result was
480 compared with synthetic deformed resected brain (ground truth) by subtracting one from another to produce a discrepancy image. If the registration result is closer to the ground truth, the discrepancy image should look smoother. Comparing Figure 7d to Figure 7e, the method with element outlier rejection demonstrates a more accurate result, which confirms our hypothesis. To quantitatively compare the two registration experiments, we used Hausdorff Distance (HD) of Canny edge points and the average distance of 6 feature points as the metrics. Please see section 3.2.1 for HD evaluation and section 3.2.2 for the feature points we choose. The results show that the removal of the elements can reduce the average HD from 4.9 mm to 3.6 mm, and reduce the average distance of feature points from 3.1mm to 1.4 mm.
485



490

495

Figure 7. The results of synthetic data. (a) Estimated source points. (b) Estimated target points. (c) Non-resected mesh M and resected mesh $M \setminus M_{Rem}$. (d) Discrepancy between non-resection and ground truth. (e) Discrepancy between resection and ground truth.

3.2 Experiments on Clinical MRI

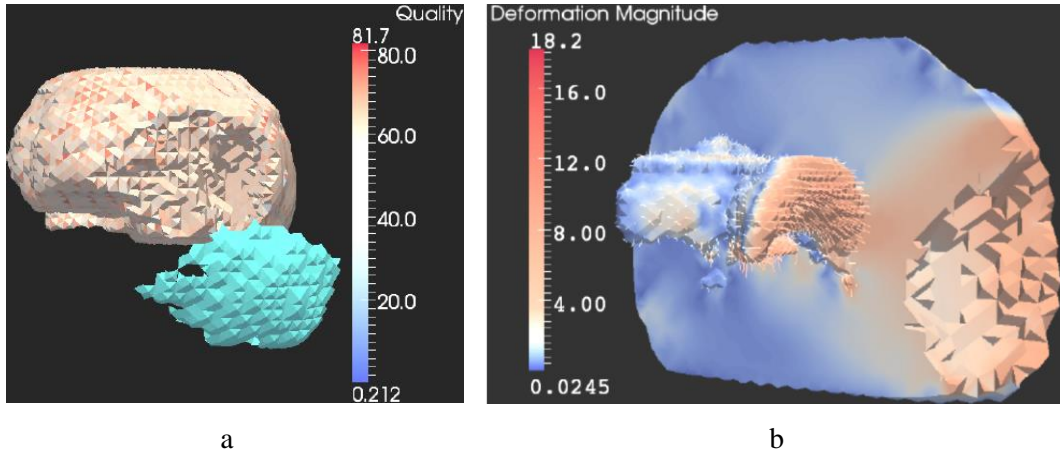
500

Figure 8a shows the resected mesh and mesh quality. The minimal dihedral angle measures the quality of the resected mesh after deformation. Figure 8b shows the deformation field of the heterogeneous model. A portion of the brain is purposely severed to expose the ventricle and its deformation field. The largest deformation reaches 18.2 mm, which occurs in the region near the resection including parts of the ventricle as the red color shows. The ventricles are squeezed inward.

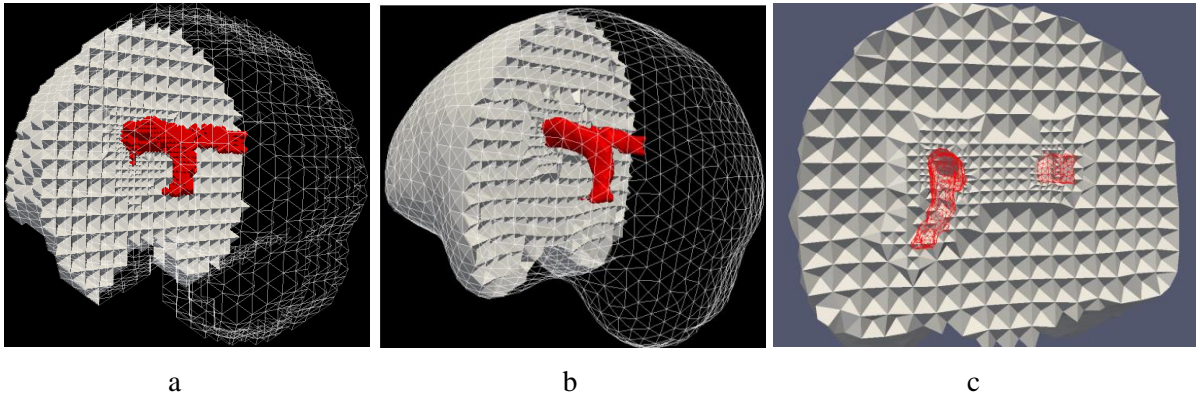
505

In this work, we compared our method with PBNRR [16], which has been implemented in ITK and released in ITK4.3 [35, 36]. PBNRR uses a homogeneous model and does not account for model resection. To compare with PBNRR, we built a simple two-tissue mesh (ventricle plus the rest of the brain) as shown in Figure 9 using our multi-tissue mesher. To specifically measure the influence of the model on the registration, we used the same multi-tissue mesh in both methods. As a result, the influence of the discrepancy of the geometry and topology between single mesh and multi-tissue mesh can be eliminated. In the homogeneous model we used Young's modulus $E = 3000\text{Pa}$, Poisson's ratio $\nu = 0.45$ for all tetrahedra, and in the heterogeneous model we replaced Young's modulus with $E = 10\text{Pa}$ and Poisson's ratio with $\nu = 0.1$ for the ventricle [15].

510



515 Figure 8. (a) Resected mesh and mesh quality after deformation. The mesh quality is measured by the minimal dihedral angle. (b) Deformation field. The color denotes deformation magnitude, and the arrow points to the deformation direction. A portion of the brain, not including ventricles, is purposely removed to display the deformation field of ventricles.



520 Figure 9. Multi-tissue mesh. (a) coarse multi-tissue mesh. (b) final multi-tissue mesh. (c) cut through of the final mesh.

525 Figure 10 shows the comparison between NEMNRR and PBNRR for two cases. We use a red arrow to point to the boundary on which NEMNRR obviously demonstrates higher accuracy than PBNRR.

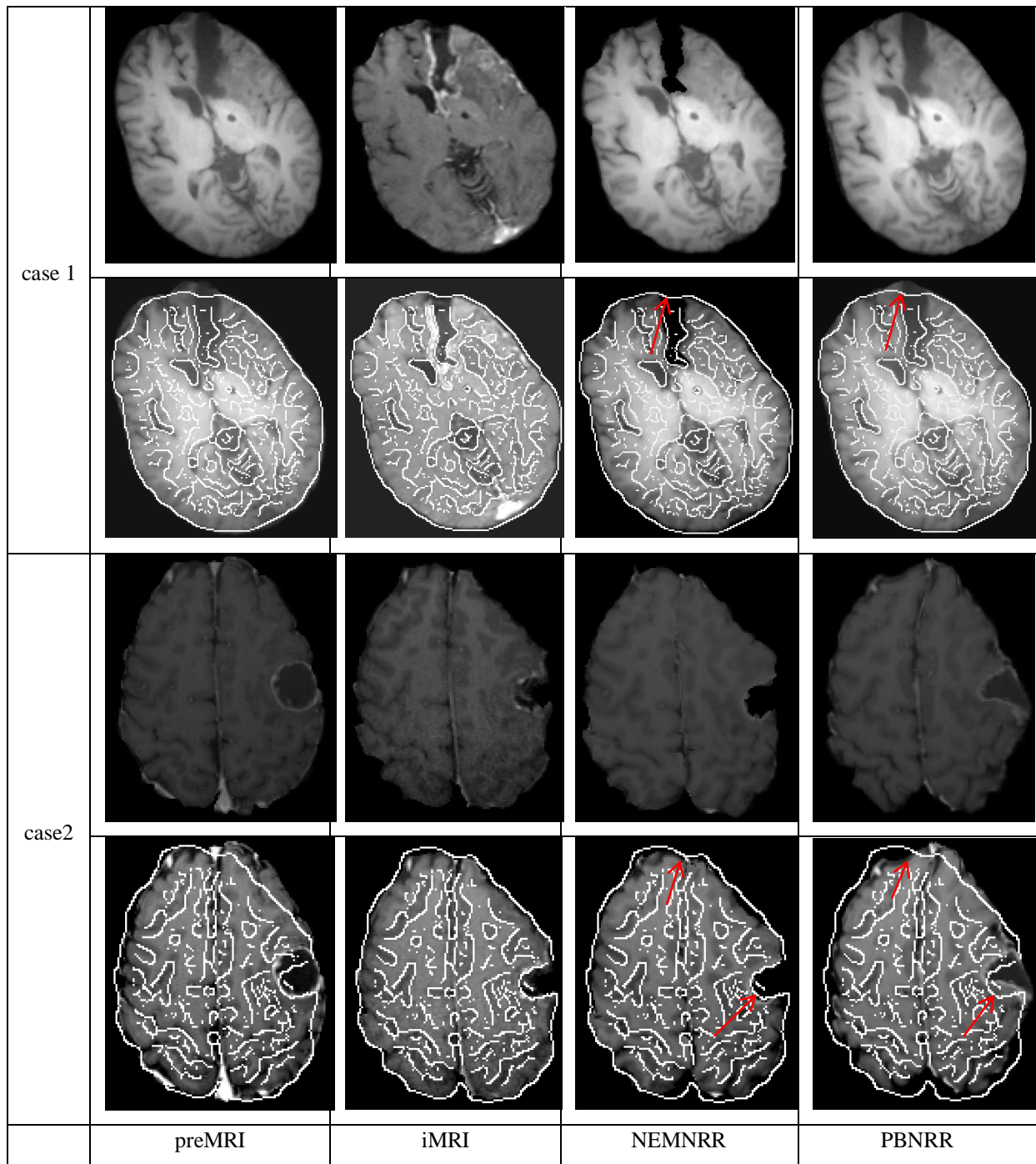
3.2.1 Quantitative evaluation with the Hausdorff Distance metric

530 To quantitatively evaluate the proposed method, we use an objective and automatic evaluation method presented in [39] for the accurate validation of intra-operative neuroimage registration. This method first uses Canny edge detection to detect two point sets, one in the aligned preoperative image and another in the intra-operative image; then excludes potential outliers with a round-trip distance larger than a prescribed threshold to get two consistent point sets; finally employs Hausdorff Distance [33] as the measurement of the degree of mismatch between two point sets with the equation,

$$H(A, B) = \max[h(A, B), h(B, A)] \quad (10)$$

where $h(A, B)$ and $h(B, A)$ are directed HD defined by $h(A, B) = \max_{a \in A} \min_{b \in B} \|a - b\|$ and

535 $h(B, A) = \max_{b \in B} \min_{a \in A} \|b - a\|$, respectively. A and B are a pair of consistent point sets.



540

Figure 10. Comparison between NEMNRR and PBNRR. The first two rows correspond to case 1 and the last two rows correspond to case 2. In each case, the first row shows rigidly aligned preMRI, iMRI, warped preMRI by NEMNRR, and warped preMRI by PBNRR, respectively. The second row shows the overlay of the edge of the iMRI on rigidly aligned preMRI, iMRI, warped preMRI by NEMNRR, and warped preMRI by PBNRR, respectively.

545

We follow the same procedures presented in [39] to do the evaluation. Table 2 shows the alignment error HD_{RR} , HD_{PBNRR} and HD_{NEMNRR} after a rigid registration (RR), PBNRR and the proposed NEMNRR method, respectively. The $Mean \pm Std$ HD value is $17.48 \pm 0.24mm$, $12.71 \pm 5.47mm$ and $9.83 \pm 4.72mm$, for the RR, PBNRR and NEMNRR, respectively.

Compared to PBNRR the NEMNRR improves the accuracy by 2.88 mm on average. When the ratio $(HD_{PBNRR} / HD_{NEMNRR}) > 1$, NEMNRR is more accurate than PBNRR. On the other hand, when $(HD_{PBNRR} / HD_{NEMNRR}) < 1$, NEMNRR is less accurate than PBNRR. According to Table 2, the NEMNRR outperforms the PBNRR with an average ratio of 1.36.

Table 2. Quantitative evaluation with the robust HD metric for 25 clinical cases. The HD_{RR} , HD_{PBNRR} and HD_{NEMNRR} (in mm) correspond to a rigid registration (RR), PBNRR and NEMNRR method, respectively. The parameters used for the PBNRR are: block radius: [1,1,1], window radius: [5,5,5], selection fraction: 0.05, rejection fraction: 0.25, number of outlier rejection steps: 10, number of approximation steps: 10. The parameters used for the NEMNRR are: $\lambda_1 = 1.0$, $\lambda_2 = 10.0$, $\varepsilon = 0.0001$, $r = 0.93$, $R = 10.0$ mm.

| Case | HD_{RR} | HD_{PBNRR} | HD_{NEMNRR} | HD_{PBNRR}/HD_{NEMNRR} |
|-------------------|------------------|------------------|-----------------|--------------------------|
| 1 | 13.41 | 7.81 | 5.00 | 1.56 |
| 2 | 23.95 | 18.38 | 16.55 | 1.11 |
| 3 | 26.43 | 20.51 | 14.56 | 1.41 |
| 4 | 8.24 | 4.12 | 4.00 | 1.03 |
| 5 | 17.00 | 10.00 | 5.38 | 1.86 |
| 6 | 9.43 | 5.00 | 4.35 | 1.15 |
| 7 | 9.69 | 7.28 | 5.00 | 1.46 |
| 8 | 6.78 | 4.35 | 4.24 | 1.03 |
| 9 | 14.45 | 9.84 | 3.74 | 2.63 |
| 10 | 13.60 | 7.48 | 6.40 | 1.17 |
| 11 | 17.72 | 12.20 | 9.00 | 1.36 |
| 12 | 21.42 | 13.15 | 9.27 | 1.42 |
| 13 | 17.83 | 10.04 | 8.06 | 1.25 |
| 14 | 24.55 | 23.04 | 17.49 | 1.32 |
| 15 | 10.67 | 7.28 | 6.40 | 1.14 |
| 16 | 21.09 | 16.52 | 8.71 | 1.90 |
| 17 | 25.61 | 21.30 | 17.14 | 1.24 |
| 18 | 12.24 | 9.69 | 7.87 | 1.23 |
| 19 | 13.15 | 6.78 | 6.40 | 1.06 |
| 20 | 32.38 | 27.36 | 26.94 | 1.02 |
| 21 | 18.68 | 12.24 | 9.16 | 1.34 |
| 22 | 19.02 | 14.31 | 12.08 | 1.18 |
| 23 | 18.05 | 17.97 | 13.92 | 1.29 |
| 24 | 27.78 | 23.00 | 19.00 | 1.21 |
| 25 | 13.92 | 8.12 | 5.09 | 1.60 |
| <i>Mean ± Std</i> | 17.48 ± 0.24 | 12.71 ± 5.47 | 9.83 ± 4.72 | 1.36 ± 0.23 |

3.2.2 Quantitative evaluation with anatomical points

To further quantitatively evaluate the proposed method, six anatomical points (A, B, C, D, E, F) were selected in the preoperative, intra-operative and warped preoperative MRI of each patient by a neurosurgery expert, as shown in Figure 11. The points A and B were selected on an individual basis at the cortex depending on the shift of the brain surface. The points C and D which could be securely

identified were chosen around the ventricular system in each dataset. The points E and F correspond to the junction between the pons and mid-brain, and the roof of fourth ventricle, respectively [41].

565

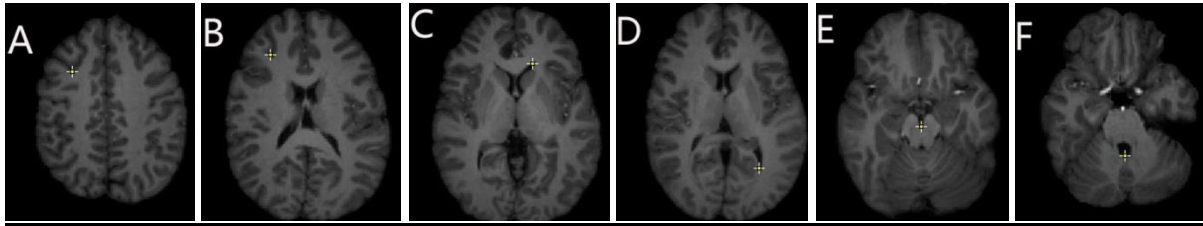


Figure 11. 6 anatomical points used for the quantitative evaluation. A and B: cortex feature points, C and D: ventricular feature points, E and F: junction between the pons and mid-brain.

570

Table 3 shows the average errors (min, max, mean) of the 25 clinical cases after the PBNRR and the NEMNRR registration. The error was calculated as the distance between the anatomical points in the intra-operative MRI and the warped preoperative MRI. For each patient, we calculated the min, max and mean errors of 6 points and then calculated their average errors, respectively for 25 patients.

575

Table 3 demonstrates that in this subjective evaluation the NEMNRR outperforms PBNRR, which is consistent with the objective evaluation using Hausdorff Distance. Compared Table 2 with Table 3, the HD evaluation shows a larger average error (9.83 mm) than the feature point based evaluation (3.69 mm). The reason is the HD measures the largest error in a huge superset (hundreds of thousands edge points) of the 6 anatomical points. The HD evaluation objectively demonstrates the proposed method outperforms PBNRR, but does not provide direct insight for the accuracy within the region of interest (ROI). In the feature point based evaluation, 6 anatomical feature points are purposely selected in the ROI suggested in [41]. The result shows the average min, max and mean errors can reach 1.36 mm, 7.79 mm and 3.69 mm, respectively, which is acceptable in clinic. Compared with a well evaluated and published method PBNRR, the proposed method increases the accuracy by 2.88

580

585

Table 3. Quantitative evaluation with anatomical points A,B,C,D,E,F for the 25 clinical cases. The error (in mm) is the distance between the identified anatomical points in the warped preoperative MRI and the intra-operative MRI.

| Method | Average min error | Average max error | Average mean error |
|--------------|-------------------|-------------------|--------------------|
| PBNRR | 2.22 | 10.10 | 5.25 |
| NEMNRR | 1.36 | 7.79 | 3.69 |
| PBNRR-NEMNRR | 0.86 | 2.31 | 1.56 |

590

4. DISCUSSION

In this paper, we use the edge points in both registration and evaluation. In the registration, the edge points are used to drive a biomechanical model to estimate the entire deformation field. The reason we

595 prefer edge points lies in the following consideration. In clinic, surgeons pay more attention to the
boundary of critical brain structures. It would be valuable to directly control the matching of the
boundary. Thus, we use Canny detection to detect the edges and then directly match the edges under
the control of the second term in energy function (6). For non-edge regions of the brain, we use a
biomechanical model (see the first term in the energy function (6)) to interpolate the deformation. In
600 another word, our method directly matches the part, in which surgeons are interested. We think this
“direct” method is better than an “indirect” method such as the intensity based method. The intensity
based method aims to match the entire intensity, but lacks the direct control of the edges, in which
surgeons are most interested. In this sense, we think incorporating edge points into the registration is
actually one advantage of our method. To make our evaluation more comprehensive, we also
605 conducted experiments using 6 anatomical points. This feature point based evaluation confirms our
method is better than PBNRR and the average mean error is acceptable in clinic.

In our work, we do not use the surface nodes of the multi-tissue mesh as the registration points. This
is due to the limitation of brain segmentation. Currently, in over 160 brain tissues, not all of them can
be precisely segmented. Thus the resulting multi-tissue mesh cannot precisely describe the geometry
610 of the brain tissues, and the surface nodes cannot provide sufficient information to drive the
biomechanical model. In this work, we only segmented the ventricles and the brain. The number of
surface nodes is much less than the number of detected edge points. So, we use the edge points
instead of the surface nodes. If many brain tissues can be segmented, we believe the edge points in the
source point set can be replaced with surface nodes.

615 In the total 25 cases, cases 4, 19 and 20 do not show obvious improvement of the accuracy.
Examining these three cases, we found all these three cases only have a very small tumor or no tumor
resected. Compared with PBNRR, one of the advantages of the proposed method lies in the removal
of elements from the biomechanical model. Because the resection region is very small or zero, the
removal of elements from the model does not affect the registration too much. Thus, the improvement
620 of the accuracy for these three cases is not obvious.

In this paper, we presented a Nested EM algorithm to resolve the three variables. We need to point out
that the proposed Nested EM cannot avoid local minima. This is because the proposed Nested EM is
based on the traditional EM, which is not a global optimizer. However, in practice, we think local
minima is not an issue because the rigid registration can bring the potential solution close to the real
625 solution.

In this work, we used a simple two-tissue heterogeneous model to perform the evaluation, but the
proposed method is capable of incorporating as many tissues as possible. We believe that as more
tissues are incorporated into the model, such as the falx of the brain, the accuracy of the registration
will be further improved.

630

5. CONCLUSION

We presented a non-rigid registration method to compensate for brain deformation resulting from tumor resection. This method does not require the point correspondence to be known in advance and
635 allows the input data to be incomplete, thus producing a more general point-based NRR. This method uses strain energy of the biomechanical model to regularize the solution. To improve the fidelity of the simulation of the underlying deformation field, we built a heterogeneous model based on a multi-tissue mesher. To resolve the deformation field with missing correspondence and resection region, we developed a Nested EM framework to resolve these three variables simultaneously.

640 Compared to an ITK implementation of a cutting edge registration method PBNRR, the NEMNRR outperforms PBNRR by improving the accuracy by 2.88 mm regarding HD evaluation, and by 1.56 mm regarding feature point evaluation on average for 25 clinical cases. The average mean error in the ROI can reach 3.69 mm.

6. ACKNOWLEDGEMENTS

645 This work is funded mainly by the ARRA funds for the ITK-V4 implementation with grant number: NLM A2D2 201000586P. In addition, this work is supported in part by NSF grants: CCF-1139864, CCF-1136538, and CSI-1136536 and by the John Simon Guggenheim Foundation and the Richard T. Cheng Endowment.

650 REFERENCES

- [1] M. I. Miga, K. D. Paulsen, J. M. Lemery, S. D. Eisner, A. Hartov, F. E. Kennedy, and D. W. Roberts, "Model-updated image guidance: initial clinical experiences with gravity-induced brain deformation," *IEEE Trans Med Imaging*, vol. 18, no. 10, pp. 866–874, 1999.
- [2] M. Ferrant, A. Nabavi, B. Macq, F. Jolesz, R. Kikinis, and S. Warfield, "Registration of 3-d intraoperative mr
655 images of the brain using a finite-element biomechanical model," *IEEE Trans Med Imaging*, vol. 20, no. 12, pp. 1384–1397, 2001.
- [3] O. Skrinjar, A. Nabavi, and J. Duncan, "Model-driven brain shift compensation," *Med Image Anal.*, vol. 6, no. 4, pp. 361–373, 2002.
- [4] Y. Liu, P. Foteinos, A. Chernikov, and N. Chrisochoides, "Multi-tissue mesh generation for brain images," in
660 *International Meshing Roundtable*, no. 19, pp. 367–384, October 2010.
- [5] M. I. Miga, D. Roberts, F. Kennedy, L. Platenik, A. Hartov, K. Lunn, and K. Paulsen, "Modeling of retraction and resection for intraoperative updating of images," *Neurosurgery*, vol. 49, no. 1, pp. 75–84, 2001.
- [6] S. Ding, M. I. Miga, J. H. Noble, A. Cao, P. Dumpuri, R. C. Thompson, and B. M. Dawant, "Semiautomatic registration of pre- and post brain tumor resection laser range data: method and validation," *IEEE Transactions on Biomedical Engineering*, vol. 56, no. 3, pp. 770–780, 2009.
- 665

- [7] A. P. Dempster, N. M. Laird, and D. B. Rubin, "Maximum likelihood from incomplete data via the em algorithm," *Journal of the Royal Statistical Society, Series B*, vol. 39, pp. 1–38, 1977.
- [8] P. Risholm, E. L. Melv er, K. M rken, and E. Samset, "Intra-operative adaptive fem-based registration accommodating tissue resection," in *Medical Imaging 2009: Image Processing*, SPIE, vol. 7259, no. 1, pp. 72
670 592Y–72 592Y–11, 2009.
- [9] C. Haili and A. Rangarajan, "A new point matching algorithm for nonrigid registration," *Comput. Vis. Image Underst.*, vol. 89, no. 2-3, pp. 114–141, 2003.
- [10] F. L. Bookstein, "Principal warps: thin-plate splines and the decomposition of deformations," *IEEE Transactions on Pattern Analysis and Machine Intelligence*, vol. 11, no. 6, pp. 567–585, 1989.
- 675 [11] P. J. Besl and N. D. McKay, "A method for registration of 3-d shapes," *IEEE Trans. Pattern Anal. Mach. Intell.*, vol. 14, no. 2, pp. 239–256, 1992.
- [12] K. Bathe, *Finite Element Procedure*. Prentice-Hall, 1996.
- [13] A. John, "R. a. fisher and the making of maximum likelihood 1912-1922," *Statistical Science*, vol. 12, no. 3, pp. 162–176, 1997.
- 680 [14] I.-F. Talos and N. Archip, "Volumetric non-rigid registration for mriguided brain tumor surgery," 08 2007.
- [15] A. Wittek, K. Miller, R. Kikinis, and S. K. Warfield, "Patient-specific model of brain deformation: Application to medical image registration," *Journal of biomechanics*, vol. 40, no. 4, pp. 919–929, 2007.
- [16] O. Clatz, H. Delingette, I.-F. Talos, A. Golby, R. Kikinis, F. Jolesz, N. Ayache, and S. Warfield, "Robust non-rigid registration to capture brain shift from intra-operative MRI," *IEEE Trans. Med. Imag.*, vol. 24, no. 11, pp.
685 1417–1427, 2005.
- [17] F. Hausdorff, *Set Theory*, 2nd ed. helsea Pub. Co., 1962.
- [18] Anand Rangarajan, Haili Chui, Fred L. Bookstein, "The softassign procrustes matching algorithm," in *Information Processing in Medical Imaging*. Springer, pp. 29–42, 1997
- [19] Y. Liu, C. Yao, L. Zhou, and N. Chrisochoides, "A point based non-rigid registration for tumor resection
690 using IMRI," in *2010 IEEE International Symposium on Biomedical Imaging: From Nano to Macro*, 2010, pp. 1217–1220.
- [20] T.J.R. Hughes, "The Finite Element Method: Linear Static and Dynamic Finite Element Analysis," Dover Publications, Mineola, pp. 207-208, 2000.
- [21] L. Vigneron, J. Verly, and S. Warfield, "Modelling surgical cuts, retractions, and resections via extended
695 finite element method resections via extended finite element method," *Int Conf Med Image Comput Comput Assist Interv*, 7(Pt 2), pp. 311-8, 2004.
- [22] S. M. Smith, "Fast robust automated brain extraction," *Human Brain Mapping*, vol. 17, no. 3, pp. 143–155, 2002.
- [23] 3DSlicer, <http://www.slicer.org/>.
- 700 [24] L. Ibanez, W. Schroeder, L. Ng, and J. Cates, "The ITK Software Guide," Kitware, Inc. ISBN 1-930934-10-6, <http://www.itk.org/>, 2003.
- [25] G. Burns and A. Glazer, *Space groups for solid state scientists*. Academic Press, 1978.

- [26] N. Molino, R. Bridson, J. Teran, and R. Fedkiw, "A crystalline, red green strategy for meshing highly deformable objects with tetrahedra," in International Meshing Roundtable, pp. 103–114, 2003.
- 705 [27] C. Haili and A. Rangarajan, "A new point matching algorithm for nonrigid registration," *Comput. Vis. Image Underst.*, vol. 89, no. 2-3, pp. 114–141, 2003.
- [28] P. J. Besl and N. D. McKay, "A method for registration of 3-d shapes," *IEEE Trans. Pattern Anal. Mach. Intell.*, vol. 14, no. 2, pp. 239–256, 1992.
- [29] Y. Liu and Z. Song, "A robust brain deformation framework based on a finite element model in igs," *The International Journal of Medical Robotics and Computer Assisted Surgery*, vol. 4, no. 2, pp. 146–157, 2008.
- 710 [30] D. Zhuang, Y. Liu, J. Wu, C. Yao, Y. Mao, C. Zhang, M. Wang, W. Wang, and L. Zhou, "A Sparse Intraoperative Data-Driven Biomechanical Model to Compensate for Brain Shift during Neuronavigation," *American Journal of Neuroradiology*, vol. 32, no. 2, p. 395, 2011.
- [31] I.-F. Talos and N. Archip, "Volumetric non-rigid registration for mri-guided brain tumor surgery,"
715 <http://www.na-mic.org/publications/item/view/541>, 2007 Aug.
- [32] N. Archip, O. Clatz, A. Fedorov, A. Kot, S. Whalen, D. Kacher, N. Chrisochoides, F. Jolesz, A. Golby, P. Black, and S. K. Warfield, "Non-rigid alignment of preoperative mri, fmri, dt-mri, with intraoperative mri for enhanced visualization and navigation in imageguided neurosurgery," *Neuroimage*, vol. 35(2), pp. 609–624, 2007.
- 720 [33] F. Hausdorff, *Set Theory*, 2nd ed. helsea Pub. Co., 1962.
- [34] P. Foteinos, Y. Liu, A. Chernikov, and N. Chrisochoides, "An evaluation of tetrahedral mesh generation for non-rigid registration of brain mri," in *Computational Biomechanics for Medicine V*, 13th International Conference on Medical Image Computing and Computer Assisted Intervention (MICCAI) Workshop, September 2010, pp. 126–137.
- 725 [35] Y. Liu, A. Kot, F. Drakopoulos, A. Fedorov, A. Enquobahrie, O. Clatz, and N. Chrisochoides, "An ITK Implementation of Physics-based Non-rigid Registration Method", *The Insight Journal*, <http://www.insight-journal.org/browse/publication/876>, 2012.
- [36] Y. Liu, and N. Chrisochoides, "Robust Scattered Data Points Approximation Using Finite Element Biomechanical Model", *The Insight Journal*, <http://www.insight-journal.org/browse/publication/872>, 2012.
- 730 [37] P. Risholm, E. Samset, I-F. Talos, Wells III W.M, "A Non-rigid Registration Framework that Accommodates Resection and Retraction," *Inf Process Med Imaging*, 21:447-58, 2009.
- [38] S. Periaswamy and H. Farid, "Medical image registration with partial data," *Medical Image Analysis*, vol. 10, pp. 452–464, 2006.
- [39] R. R. Garlapati, G. R. Joldes, A. Wittek, J. Lam, N. Weisenfeld, A. Hans, S. K. Warfield, R. Kikinis, and K.
735 Miller, "Objective evaluation of accuracy of intraoperative neuroimage registration," accepted by *Computational Biomechanics for Medicine workshop*, MICCAI 2012.
- [40] Yixun Liu, Panagiotis Foteinos, Andrey Chernikov, Nikos Chrisochoides, "Mesh deformation based multi-tissue mesh generation for brain Images," *Engineering with Computers*, Volume 28, Issue 4, page 305-318, 2012.

740 [41] P. Hastreiter, C. Rezk-Salama, G. Soza, M. Bauer, G. Greiner, R. Fahlbusch, O. Ganslandt, and C. Nimsky, "Strategies for brain shift evaluation," Medical Image Analysis, vol. 8, no. 4, pp. 447-464, 2004.